Chapter 5
Deformation Behaviors

5.1 Elastic Moduli

Elastic moduli that characterize the linear relationship between stress and strain express the shape of the potential energy of an atom-pair in materials. If solute hydrogen alters the distance or the cohesive force between neighboring host atoms, its effects are expected to appear in elastic moduli. The effects of hydrogen on Young's modulus of polycrystalline bcc tantalum, niobium and vanadium were measured from the velocity of 100 kHz elastic wave in wire specimens [1]. Hydrogen was cathodically charged in 4 % sulfuric electrolyte with small amounts of CS_2 and As_2O_3. Numerical values of hydrogen contents were not shown, but a linear increase in Young's modulus E with hydrogen content was reported for each metal. The increases in terms of $\Delta E/E$ were 0.07, 0.58 and 0.48 % for Ta, Nb and V, respectively, per 1 at % of hydrogen. On the contrary, a linear decrease in Young's modulus against the square root of the hydrogen concentration up to 2.5×10^{-3} was reported for a Ti-Mo alloy accompanying solution softening and expansion of lattice parameter [2].

The solid solubility of hydrogen in α-iron at room temperature is normally very low as described in Chap. 1, and the expected changes of moduli, if any, are also very small. The measurements of shear modulus of hydrogen-charged polycrystalline α-iron by means of a torsion pendulum method showed a decrease of about 0.3 % of the pendulum frequency at temperatures lower than 200 K [3]. For the experiment, hydrogen was introduced by electric discharge of wet hydrogen gas. The hydrogen concentration was not exact, but an estimated decrease in the shear modulus of iron by 1 at % hydrogen was about 8 % at 100 K.

M. Nagumo, *Fundamentals of Hydrogen Embrittlement*,
DOI 10.1007/978-981-10-0161-1_5

5.2 Flow Stress

Lattice distortion around solute hydrogen atoms and resulted interactions between dislocations and hydrogen, described in Sect. 3.1, may cause solid solution hardening or softening. However, the low concentrations of hydrogen and trapping in various lattice defects often make precise arguments difficult. For a Ti-Mo alloy cited above [2], the proportional limit and 0.2 % proof stress decreased linearly against the square root of hydrogen concentration. For iron and steels, hydrogen effects are fairly complicated depending on materials, deformation stages and testing conditions. Hydrogen effects on the flow stress of iron are not yet conclusive, and Table 5.1 summarizes reported results in the literature [4–15].

(a) Hardening

Hardening by hydrogen is more general than softening for commercially pure iron, low-alloyed and stainless steels tested for bulky specimens at room temperature. For iron single crystal containing about 50 ppm or less of carbon, the critical resolved shear stress for yielding increased on $\{110\} < 111 >$ slip system in a hydrogen precharged specimen, while it was almost immune on $\{112\} < 111 >$ slip system [4]. The tensile straining was conducted at room temperature at strain rates of about 10^{-4}–10^{-5}/s using specimens of 2 mm in thickness. The effects of hydrogen on hardening behaviors vary by carbon contents. For carbon-doped iron single crystals, flow stress increased by 165 ppm carbon but decreased by 10 ppm on tensile straining in the presence of hydrogen [7]. For an intermediate 90 ppm carbon, the flow stress was higher or lower than that of the hydrogen-free specimen according to strain ranges less or larger than about 30 %, respectively. For the experiments, tensile straining was conducted setting the tensile axis near $<001>$ at room temperature under cathodic electrolysis.

For polycrystalline iron containing 10 ppm carbon and ~30 μm in grain size, the yield and flow stress increased by hydrogen on tensile straining of specimens of 2 mm in thickness [8]. For the experiments, hydrogen of ~2 ppm was precharged in 0.1 MPa hydrogen gas at 850 °C and tensile tests were conducted at 0 °C and −80 °C. A noteworthy fact was that hydrogen enhanced the increase in the flow stress by strain aging at low strains less than 5 %.

The grain size dependence of hydrogen effects was also examined in terms of the Hall–Petch relation for the grain size range of 10 ~ 150 μm with commercial pure iron [9]. Tensile tests were conducted at room temperature under cathodic hydrogen-charging to 2–7 ppm in the average hydrogen concentration. The 0.5 % offset stress decreased by hydrogen for coarse grain sizes over ~30 μm but increased for finer grain sizes. However, for iron in which interstitial impurities were reduced by adding 0.15 % titanium as a getter, reductions of the strength by hydrogen were observed for all grain sizes.

The effects of specimen thickness on flow stress at room temperature were examined with a decarbulized rimmed steel containing ~40 ppm of carbon [10]. The flow stress always increased for specimens of 0.8 mm in thickness

Table 5.1 Effects of hydrogen on the flow stress of iron

	Specimen			H-Charging	Strain Rate (s^{-1})	Temperature	Hydrogen Effects	Ref.
	Purity	Grain Size	Size (t × w)					
1	Decaborized Armco iron (C: 30 ~ 50 ppm)	single crystal	2 × 2 mm	1 N HCl aq + hydrazine 30 A/m^2	3.3×10^{-4}, 3.3×10^{-5}	RT	Hardening for: {110} < 111>, Small change for {112} < 111>	[4]
2	Zone-refined pure iron	single crystal	1.5 mmφ	1 N H_2SO_4+ As_2O_3 40 A/m^2	4×10^{-4}	RT	Softening	[5]
3	Zone-refined pure iron (Resistance ratio 4700)	single crystal	0.4φ or 0.1 × 1.4	0.1 N CH_3OH – H_2O – H_2SO_4 20 or 40 A/m^2	8.3×10^{-4}	200 K	Softening, but hardening in the 3rd work-hardening stage	[6]
4	Zone-refined pure iron (Varied C contents)	single crystal	– TA //<001>	1 N H_2SO_4+ As_2O_3	–	RT	Softening in the 1st and 2nd work hardening stages. Hardening when C is added	[7]
5	Vacuum melt electrolytic iron	30 μm	2 × 5 mm	1 atm H_2, 850 °C × 1 h → liq. N_2	6×10^{-4}	0 °C ~ -80 °C	Hardening, prominently at ε < 8 %	[8]
6	Decarbolized Ferrovac E	10 ~ 150 μm	-	1 N H_2SO_4+ As 10 A/m^2	6.5×10^{-3}	RT	Enhanced grain-size dependence of proof stress. Hardening for fine grain size less than 30 μm	[9]
7	Remelt Plasitron (added 0.15%Ti)	10 ~ 150 μm	–	1 N H_2SO_4+ As 10 A/m^2	6.5×10^{-3}	RT	Softening	[9]

(continued)

Table 5.1 (continued)

	Specimen			H-Charging	Strain Rate (s^{-1})	Temperature	Hydrogen Effects	Ref.
	Purity	Grain Size	Size (t × w)					
8	Vacuum melt mild steel and pure iron	20 μm	0.06 ~ 0.8 × 6 mm	1 N $H_2SO_4 + As_2O_3$ 10 A/m^2	3.3×10^{-5}	RT	Hardening, but softening for fine specimen size less than 0.19 mm	[10]
9	Zone-refined pure iron (Resistance Ratio 3500 ~ 6000)	0.3 mm (RRR 3600) 1.0 mm (RRR 5000)	0. 4 mmφ	0.1 N NaOH + Na_2AsO_2 100 or 300 A/m^2	8.3×10^{-5}	170 ~ 297 K	Softening, but hardening even at 200 k for low purity iron. Enhanced softening at lower strain rate	[11]
10	Zone-refined pure iron (Resistance Ratio 1800 ~ 5000)	0.1 mm (RRR 1800) 0.3 mm (RRR 3600) 1.0 mm (RRR 5000)	0. 4 mmφ	0.1 N CH_3OH - H_2O - H_2SO_4 20 or 40 A/m^2	8.3×10^{-5}	170 ~ 297 K	Softening reduced at elevating temperatures. Hardening at room temperature for low purity iron	[12]
11	Zone-refined pure iron +0.6 at %Ti Zone-refined pure iron +0.2 at%Mo	60 ~ 100 μm	0. 5 mmφ	*ibid*	3.3×10^{-5}	200 ~ RT	Hardening for Fe-T. Hardening at RT but softening at below 0 °C for Fe-Mo	[13]
12	Zone-refined pure iron (Resistance Ratio 3600 ~ 5200)	0.4, 1.0, 2.0 mm	0. 4 mmφ	*ibid*	$1.7 \times 10^{-3} \sim 8.3 \times 10^{-5}$	170 ~ 297 K	Softening reduced by increasing strain rate and current density	[14]
13	Remelt electrolytic iron	Single crystal	TA // <110> (0.1–1.0) × 5 mm	C_2H_5OH + H_2SO_4 50 A/m^2	5×10^{-5}	195 K	Enhanced softening for smaller specimen size	[15]

The residual resistance ratio (RRR) is a measure of the purity of material defined as the ratio of electric resistivity at room temperature and that at 4.2 K

when the cathodic current for hydrogen-charging was switched on during tensile straining. However, the flow stress turned to decrease with strain by reducing specimen thickness and softening appeared for the thickness less than 0.20 mm. On the other hand, hardening was always the case for 17Cr steel.

Hardening by hydrogen was also observed for a commercial quenched and tempered steel [8] and a Fe-0.5%Ti alloy [13] on tensile straining at temperatures below room temperature. Another demonstration of hardening was that two-stage Lüders deformation appeared on tensile straining of commercial 1045 steels [16]. For the experiment, hydrogen was introduced into one half of the gauge section, and the second stage Lüders deformation was deduced to arise from the yielding of the hydrogen-charged portion.

(b) Softening

On the other hand, softening by hydrogen generally appears for thin specimens of high purity iron at temperatures below room temperatures. Figure 5.1 [12] shows tensile stress–strain curves of zone-refined high purity iron specimens of 0.4 mm in diameter tested at low temperatures. Upward and downward arrows indicate, respectively, switching on and off of cathodic current for hydrogen charging. While only hardening by hydrogen was observed at room temperature, a gradual decrease of flow stress after a small hump or a prompt decrease appeared at lower test temperatures. It is to be noticed that the decrease in the flow stress at the start of hydrogen charging was temporal at temperatures lower than 180 K and the flow

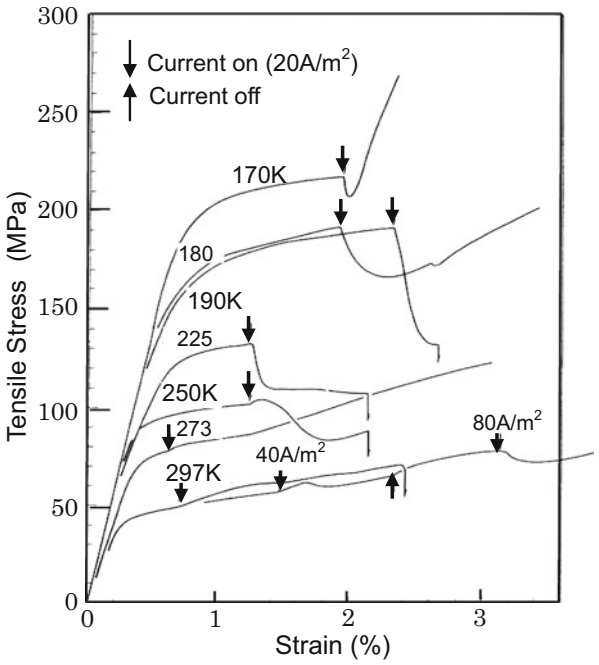

Fig. 5.1 Effects of cathodic polarization on tensile curves of pure iron specimens at different temperatures (Matsui et al. [12])

stress tended to increase again at 170 K. The decrease in the flow stress on hydrogen charging at low temperatures was more prominent for higher purity iron. The amount of softening depends on test conditions. The difference in the flow stresses between the final steady level and before charging increased with the higher charging current density, the lower strain rate and the smaller specimen size [14]. It is to be noted that microstructures of the coarse-grain specimens were bamboo-like.

Softening by hydrogen was also observed for tensile straining of single crystal iron specimens as thick as 3 mm in diameter at room temperature and within the easy glide region under continuous hydrogen charging [17]. Slip markings on the specimen surface were finer for hydrogen-charged specimens than those of the hydrogen-free ones. According to the shear stress *vs*. shear strain curve, work-hardening rate soon after yielding increased in the presence of hydrogen and shear stress exceeded that of hydrogen-free specimens, *i.e*. softening turned to hardening. The critical resolved shear stress for yielding was, however, almost the same for specimens with/without hydrogen charging. Softening was also observed over a wide range of strain at 200 K for a single crystal iron specimen of 2 mm in thickness, but a polycrystalline iron showed hardening in small strains less than 5 % [18].

Softening by hydrogen is more prominent for lower strain rates. Figure 5.2 [11] shows the temperature dependence of the yield stress of high purity iron tested at different strain rates. For the experiments, the specimens of 0.4 mm in diameter were prestrained to 1–2 % and hydrogen-precharged by cathodic electrolysis. The

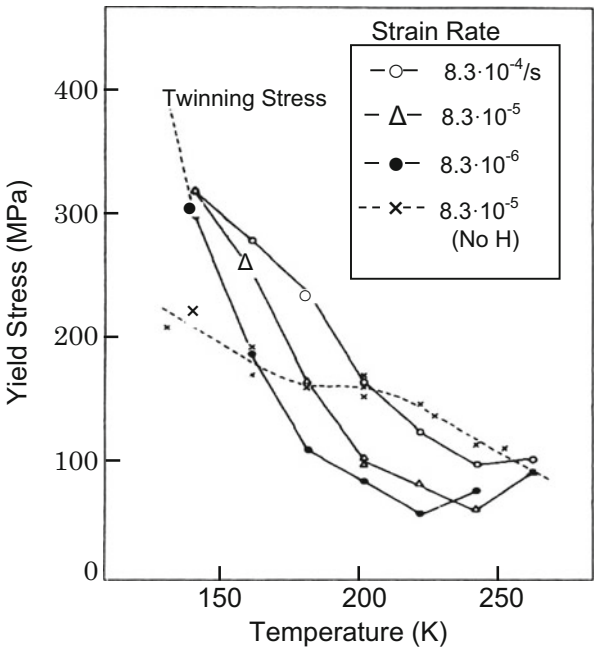

Fig. 5.2 Yield stress of prestrained and hydrogen-precharged iron at different strain rates and temperatures. The broken line is for specimens without hydrogen (Moriya et al. [11])

yield stress increased with decreasing temperature and exceeded the yield stress of the hydrogen-free specimens, *i.e.* turned to hardening by hydrogen. It is noticed that prestraining introduces fresh dislocations in specimens. Aging of prestrained and hydrogen precharged specimens at room temperature diminished hydrogen effects on the yield stress or rather showed hardening at 200 K even at the strain rate of 8×10^{-5}/s [11].

Softening by hydrogen was reported earlier as a pronounced decrease of torque in torsion tests of mild steel tubes [19]. The specimen was a tube of 2 mm in wall thickness and 20 mm in outer diameter. The test was conducted at room temperature, and hydrogen was introduced by immersing the specimen in 5 % H_2SO_4 with small additions of poisons. The observed softening and fractographic features described in Sect. 7.1(f) are the basis of the hydrogen-assisted cracking (HAC) model for the mechanism of hydrogen embrittlement described in Sect. 10.2.

(c) Explanations of experimental results

Observed changes of flow stress induced by hydrogen charging are complicated as described above, depending on the purity, grain size, specimen size, testing temperature, strain rate and fugacity of hydrogen. Hydrogen effects for softening have been discussed so far with respect to (1) interactions of hydrogen with dislocations, (2) the increase in the density of mobile dislocations or (3) the formation of damage in near-surface areas. In many experiments, hydrogen was introduced into specimen using cathodic electrolysis under fairly high fugacity of hydrogen as shown in Table 1.1. It is to be noticed, however, that direct evidences for supposed mechanisms are scarce and quantitative theoretical estimations are difficult.

The motion of screw dislocations dominates plastic deformation after pre-yield strain for iron single crystal at low temperatures. The Peierls potential for screw dislocations in bcc metals is high and strain rate is controlled by the formation of kink-pairs and the side-way movement of kinks. To explain softening observed for high purity iron, Matsui et al. postulated that hydrogen enters the dislocation core and modifies the core structure to increase the double kink nucleation rate [12]. A prompt response of the flow stress to cathodic polarization was ascribed to the transportation of hydrogen by moving dislocations. Experimental conditions employed by Matsui et al. were characterized by high hydrogen fugacity, extremely high purity, and also coarse-grain thin specimens. High concentrations of hydrogen far exceeding equilibrium may exhibit solid solution hardening or softening in similar ways as carbon and nitrogen play their roles. However, Matsui et al. ruled out this possibility for tests at temperatures at which hydrogen was mobile together with dislocations. They assumed that interactions between hydrogen and impurities cause hardening at and above 273 K in impure specimens containing dissolved impurities comparable in concentrations to hydrogen. First-principles calculations for interactions of hydrogen with the core of screw dislocations and for their role on the mobility of dislocations are presented in Sects. 3.1.2 and 5.5, respectively.

On the other hand, Lunarska et al. suggested that softening by hydrogen in the easy glide region at room temperature was due to long-range internal stress rather than double kink formation, because the critical resolved shear stress for yielding

was unaffected by hydrogen charging [17]. The proposed mechanism was that the segregation of hydrogen around dislocations lowered elastic interactions between dislocations. On the other hand, hydrogen effects were featured by fine slip markings and higher work-hardening rate leading to hardening in Stage III. Lunarska et al. also suggested the formation of some obstacles against dislocation motion. Hydrogen effects on enhancing the mobility of dislocations are also discussed with respect to shielding of elastic fields by hydrogen as described in Sect. 5.5.1 concerning direct observations by transmission electron microscopy. Hydrogen-enhanced strain localization (HELP) associated with the formation of defects is described in Sect. 7.2.1.

High hydrogen fugacity eventually induces surface damage and actually some blisters appear on the surface of hydrogen-charged specimens [12]. Oriani and Josephic noticed that the generation of blisters or microvoids themselves causes softening by reducing localized stress at the sites and thus increasing the effective stress [16]. They also noticed that the surface of microvoids might facilitate deformation by serving as additional source and sinks of dislocations, increasing the number of mobile dislocations and reducing the number of dislocation pile-up. On the other hand for hardening effects by hydrogen, Oriani and Josephic proposed that hydrogen reduces stacking fault energy that impedes cross slipping. Suppression of the dislocation nucleation from grain boundaries and their ledges was another mechanism Oriani and Josephic proposed for hardening.

The specimen size dependence of softening [10] is a support for surface effects originating in flaw induced by hydrogen charging. However, softening appeared even under mild hydrogen-charging conditions by which the formation of blisters is unlikely [11]. Changes of stress–strain curves associated with switching on and off of charging current are too complicated to simply ascribe to the formation of blisters or voids. An important viewpoint not so much paid attention so far on the flow stress under concurrent electrolysis is the decrease in surface energy due to adsorption of hydrogen on the surface. Surface effects are viable for experiments using thin specimens. As shortly described in following sections, surface effects likely operate in stress relaxation, creep and dislocation mobility under *in situ* transmission electron microscopy. Generation of dislocations from the surface and associated changes of internal dislocation structures should be considered.

An important aspect to be not disregarded on functions of hydrogen associated with the movement of dislocations is the creation of point defects. Moving dislocations multiply dislocations, and screw dislocations gliding on a slip plane generate jogs by intersecting screw dislocations on other slip planes. Transmission electron microscopy applied to deformation microstructures revealed large jogs forming dipoles of edge dislocations for a single crystal of 3 % Si iron [20], and the formation of tangles and cells of dislocations in iron single crystals as a result of mutual interactions of dislocations [21]. The interactions of dislocations with other lattice defects are important factors controlling the flow stress. The interactions of hydrogen with lattice defects created by moving dislocations besides with dislocations are important particularly in areas when the density of dislocations is substantial. The interactions of hydrogen with vacancies created by dragging of jog are described in Sect. 3.2.3.

5.3 Stress Relaxation and Creep

5.3.1 Stress Relaxation

Stress relaxation is a partial release of external stress under a constant strain. An example of stress relaxation in engineering practice is the loss of compacting stress in prestressed steel structures. Stress relaxation eventually leads to fracture. The delayed fracture of steel components stressed at constant displacement in corrosive environments is a case associated with hydrogen-assisted stress relaxation.

Dislocation configurations forming under rising stress turn towards stable structures on stopping the stress increase. At a constant-strain state, the macroscopic strain-rate is zero, *i.e.*

$$\varepsilon = \varepsilon_{\mathrm{e}} + \varepsilon_{\mathrm{p}} = \mathrm{const}, \tag{5.1}$$

then

$$\dot{\varepsilon}_p = -\dot{\varepsilon}_e = -\frac{\dot{\sigma}_e}{E}, \tag{5.2}$$

where suffixes e and p denote elastic and plastic, respectively, and E is Young's modulus. Equation (5.2) implies that plastic strain-rate associated with the rearrangement of dislocations appears as a decrease of elastic stress-rate. Stress relaxation originates in microplasticity and is a measure of the stability of microstructures, particularly of configurations of dislocations. The relaxation rate is very susceptible to temperature variation and its measurement must be conducted under a careful temperature control.

According to dislocation theory of plasticity, the plastic strain-rate is expressed as

$$\dot{\varepsilon}_p = \varphi\rho b\overline{v}, \tag{5.3}$$

where φ is a geometric factor, ρ is the density of mobile dislocations, b is their Burgers vector and $\overline{v}$ is the average velocity of dislocations. When the viscous flow model of dislocations [22] is employed, $\overline{v}$ is expressed as

$$\overline{v} = A(\tau - \tau_i)^m, \tag{5.4}$$

where A is the average velocity at unit effective stress, τ is the applied shear stress, τ_{i} is the internal shear stress and m is the dislocation velocity-stress exponent. Equation (5.2) is written using Eqs. (5.3) and (5.4) as

$$\dot{\varepsilon}_p = -K\rho(\tau - \tau_i)^m, \tag{5.5}$$

where K is a constant [23]. Then, hydrogen effects in stress relaxation are related to the density of mobile dislocations, the magnitude of internal stress and m.

Hydrogen enhances stress relaxation. Stress relaxation of a zone-refined pure iron in the uniform elongation region shows a substantially enhanced load drop when cathodic hydrogen charging is applied [24]. Figure 5.3 [24] shows hydrogen effects on deformation parameters in Eq. (5.4) obtained by stress relaxation experiments for coarse-grain pure iron at room temperature. Stress relaxation was started at different initial tensile strains ε_0 and hydrogen charging was applied some 1.5–5 min after the start of stress relaxation using cathodic electrolysis in poisoned 1 N H_2SO_4 at a current density of 20–170 A/m^2. The results of Fig. 5.3 indicate that hydrogen reduces internal stress and the dislocation velocity-stress exponent m in Eq. (5.4). Hydrogen fugacity in that experiment was fairly high while data were collected before the formation of blisters.

Reduction of the current density or interruption of charging resulted in an increase of load, and the restart of the cross-head motion showed a jump-like increase in load. Similar hydrogen effects in stress relaxation were observed for many types of iron and steels. Figure 5.4 [10] shows effects of charging current on

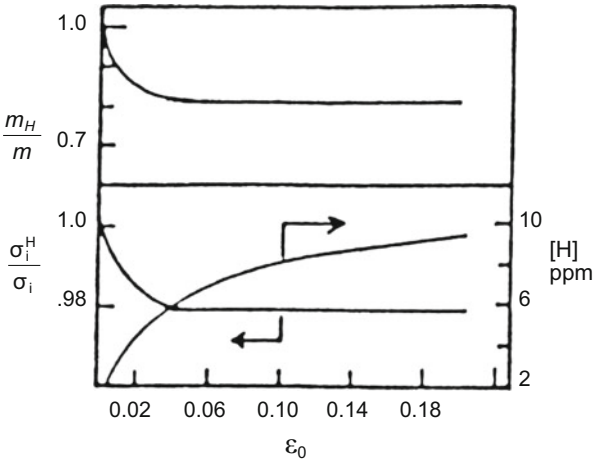

Fig. 5.3 Deformation parameters in Eq. (5.4) for coarse-grain pure iron at stress relaxation tests from different initial strains ε_0 with and without hydrogen-charging. Hydrogen-charging current is 3.8 mA/cm^2 (Lunarska [24])

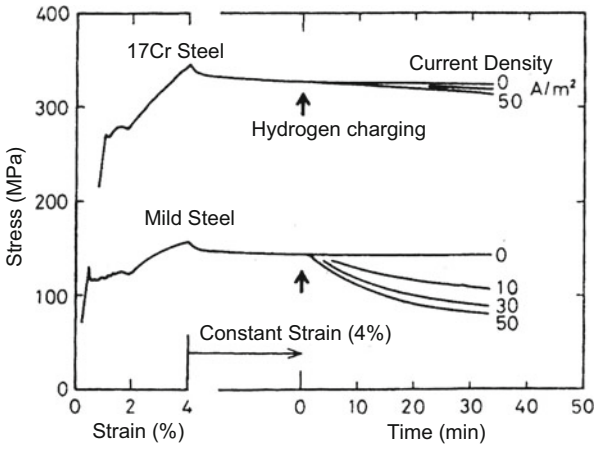

Fig. 5.4 Stress relaxation curves of mild steel and 17Cr steel specimens started at constant strain of 4 %. Cathodic electrolysis was applied in the course of stress relaxation (Asano et al. [10]. Reprinted with permission from Japan Inst. Metals)

enhancing stress relaxation for decarbulized rimmed steel and 17Cr steel. Cathodic polarization was applied during stress relaxation at a constant strain of 4 %. The thickness of the specimen in Fig. 5.4 was 0.8 mm, but the enhancement was more prominent for thinner specimens [10], similarly to the flow stress on tensile straining.

The magnitude of the charging current density is related to hydrogen fugacity that determines solid solubility of hydrogen (Sect. 2.1.1). Oriani and Josephic showed a threshold of the input hydrogen fugacity, *i.e.* some critical hydrogen charging current density, for inducing an abrupt increase in the relaxation rate [25]. The threshold fugacity was higher for higher initial plastic strain to start stress relaxation. On the other hand, a well-defined effect by hydrogen was not discernible on the slope of the relaxation curve at initial strain below a certain amount. The experiments were conducted for AISI 1045 steels 0.25 mm in thickness at room temperature under a careful temperature control. Preceding experiments for flow stress and stress relaxation mostly employed hydrogen charging under fairly high fugacity, but Oriani and Josephic used poisoned 0.1 N NaOH for electrolyte at very low current density and the estimated threshold fugacity was several MPa. The mechanism was discussed in terms of hydrogen-assisted nucleation and growth of microvoids due to decohesion of atomic bonds.

The enhancement of stress relaxation appears not only at simultaneous hydrogen charging during stress relaxation but also by precharged hydrogen. Figure 5.5 [26] shows stress relaxation curves of a 0.37%C-0.6%Si-1.0%Mo-0.5%Cr-0.54 V martensitic steel tempered at 550 °C and 650 °C. Secondary hardening due to the precipitation of fine vanadium carbides by tempering at 650 °C coupled with advanced recovery of martensite gave the same tensile strength of 1470 MPa as that for specimens tempered at 550 °C. Hydrogen precharging was conducted in a mild condition using cathodic electrolysis in a 3 % NaCl + 3 g/*l* NH_4SCN solution at a current density of 5 A/m^2. The specimens were 2 mm in thickness and stress relaxation at 28 ± 0.5 °C was started by stopping tensile straining at 60 % of the

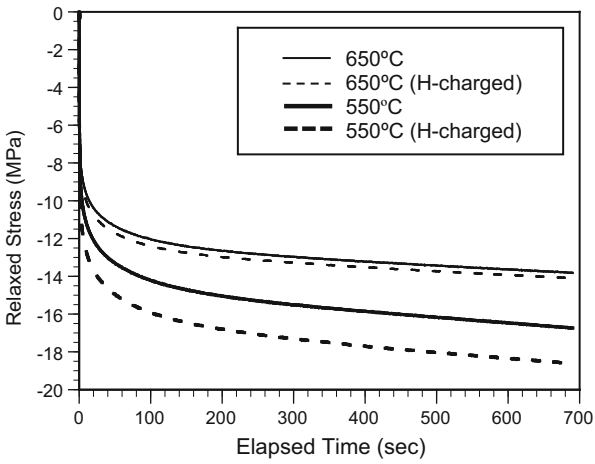

Fig. 5.5 Effects of hydrogen-precharging on stress relaxation curves of Mo-V martensitic steel specimens tempered at 550 and 650 °C. The initial stress is 0.6 of the tensile strength and the test temperature is 28 ± 0.5 °C (Nagumo et al. [26])

ultimate tensile strength. Enhancement of stress relaxation by hydrogen was observed for both tempering temperatures, but tempering at 650 °C substantially reduced the extent of relaxation. It is likely that more stable microstructures of martensite formed by the higher tempering temperature coupled with homogeneous distributions of vanadium carbides suppress strain localization and reduce associated plastic strain rates.

A noteworthy fact concerning the relevance of stress relaxation to hydrogen embrittlement was that tempering of the Mo-V steel at 650 °C improved the resistance to delayed fracture compared with tempering at 550 °C [26]. Relevance of stress-relaxation rates to the susceptibilities to delayed fracture is likely a general feature for steels of similar strength levels or chemical compositions. Early studies revealed a high resistance to delayed fracture and a very small stress relaxation in an 18Ni maraging steel [27]. A correlation between stress relaxation rate and the time to fracture in delayed fracture tests was found for low carbon martensitic steels [28]. Relevance of stress relaxation to hydrogen embrittlement for the Mo-V steel is described in Sects. 6.4.2 and 8.1(b).

5.3.2 Creep

Creep is time-dependent plasticity under constant load or stress and is particularly important for the high-temperature engineering life of materials. At elevated temperatures, sliding of grain boundaries or diffusion of vacancies are primary origins of creep failure. Creep strain is normally very small at room temperature, but delayed fracture under constant stress is a phenomenon accompanying creep. Various mechanisms operate according to types of materials, applied stress and temperatures [29]. Motion of dislocations induced by external stress is opposed by internal stress and obstacles. However, thermal energy gives rise to activation of dislocations or other elements that have been equilibrated under an applied stress and causes microplasticity.

The general form of creep curve is schematically shown in Fig. 5.6, and it depends on temperature and applied stress. The creep curve is generally composed

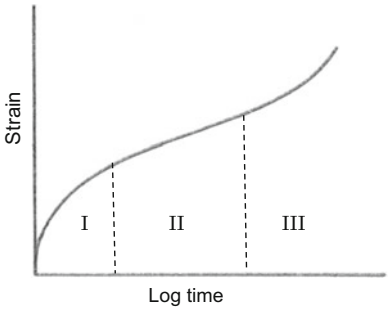

Fig. 5.6 Schematic illustration of three stages in creep curve

of three stages, the transient creep stage of decelerating flow, the steady-state creep of a constant minimum rate and eventually at high temperatures the stage of accelerating flow that ends in fracture. The exhaustion theory of transient creep is that each element is thermally activated only once by a characteristic activation stress and contributes to plastic strain [29]. The creep rate in the transient and steady-state stages is expressed as

$$\dot{\varepsilon} = At^{-n}, \tag{5.6}$$

where A and n are constants and $0 < n < 1$. The steady-state creep rate increases strongly with temperature. The rate over a small range of stress is expressed in terms of the activation energy of dislocation movement in the form of

$$\dot{\varepsilon} = K\exp\left(-\frac{U - b\sigma}{RT}\right), \tag{5.7}$$

where K, U and b are constants. A refined form of the activation energy was derived by Cottrell considering dislocation movement passing through closely spaced obstacles, like dislocation forests [30]. Preceding studies about hydrogen effects descried below, however, were developed before this consideration was presented.

Hydrogen effects on the density, mobility and barriers to movement of mobile dislocations are to appear on creep behaviors while experiments on this matter are not many. Creep rates are higher for higher hydrogen concentrations, similarly to the stress relaxation test shown in Fig. 5.4. During creep deformation of a single crystal specimen of pure iron at 200 K, a sudden application of cathodic potential was insignificant to the creep rate when the potential was low. At a higher applied potential, acceleration of creep rate appeared initially gradually then rapidly and finally to a nearly steady state [18]. In the experiments by Park et al., the thickness of the specimens was 0.8 mm and the applied stress was 60 % of the yield stress. Hydrogen effects were more prominent at higher current densities and stress levels, but the acceleration decreased with increasing temperature and was insignificant at room temperature. When the potential was turned off, the creep rate returned in a few minutes to the initial value before cathodic charging. Such temperature dependence of the accelerated creep rate is similar to softening of the flow stress shown in Fig. 5.1.

The threshold fugacity for accelerating creep rate was also found by Oriani and Josephic with spheroidized AISI 1040 steel [31] by a similar method as used for stress relaxation [25]. The wire specimen was 0.12 mm in diameter and hydrogen charging was conducted by cathodic electrolysis in poisoned 0.1 N NaOH aqueous solution at room temperature. The creep rate at room temperature increased abruptly on applying cathodic potential above a critical value. The increase then decelerated following the form of

$$\varepsilon - \varepsilon_0 = k\ln(t - t_0). \tag{5.8}$$

Shut off of the charging current raised markedly the creep rate to a maximum and then the rate decreased. Oriani and Josephic considered the function of hydrogen similar to that in stress relaxation [25], *i.e.* the reduction in internal stress by the

nucleation and growth of microvoids induced by the reduced cohesive strength by hydrogen.

Contribution of vacancies to creep becomes significant with elevating temperatures. If hydrogen increased the density of vacancies as described in Sect. 3.2.3, hydrogen might increase creep rate. Actually, the creep rate at 736 ~ 1200 K of a Pd wire of 0.1 mm in diameter was about six times higher in a 0.1 MPa H_2 atmosphere than that in an Ar atmosphere of the same pressure [32]. Hydrogen reduced the creep activation energy from 38.6 ± 1.9 kJ/mol in Ar gas to 30.0 ± 1.5 kJ/mol in H_2 gas. However, the mechanism of the observed creep was ascribed to grain boundary diffusion of Pd atoms and the effect of hydrogen on the diffusion of Pd atoms was not discussed.

5.3.3 *Implications of Surface Effects*

The effects of hydrogen on stress relaxation and creep have been discussed mostly with respect to interactions of hydrogen with moving dislocations in specimens and also to surface damage induced by a high hydrogen fugacity. Cathodic polarization introduces hydrogen into metals, but anodic polarization also increases creep rate. Figure 5.7 [33] compares creep curves of a thin copper wire for (a) anodic and

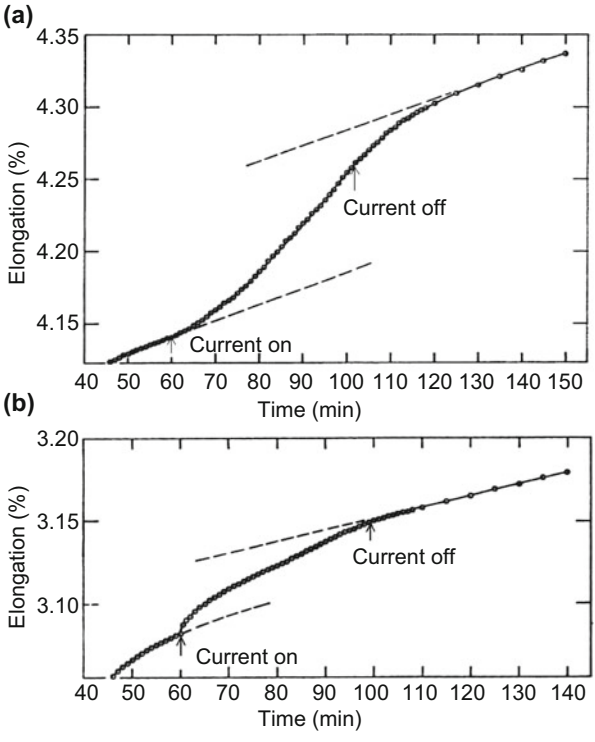

Fig. 5.7 Effects of polarization on creep curves of Cu wire at room temperature. The diameter of wires is 0.27 mm, and the applied stress is 90 MPa. (**a**) anodic polarization, and (**b**) cathodic polarization (Revie et al. [33])

(b) cathodic polarizations. The average grain size was about 20 μm and the diameter of the wire was 0.27 mm. The electrolyte was an aqueous acetate buffer solution of pH 3.7 at 25 ± 0.5 °C and the current density was 9 A/m^2. Both cathodic and anodic polarizations increased creep rate. Anodic polarization increased the creep rate gradually and shutting-off of the current decreased the rate to a level similar to that before the application of polarization. On the other hand, cathodic polarization also increased the creep rate to the same order as anodic polarization, but the increase in creep rate was abrupt on the application of polarization.

The increase in creep rate by both anodic and cathodic polarizations implies that some factors other than hydrogen affect creep rate associated with chemical reactions on the specimen surface. On anodic polarization estimated thinning of the wire was not significant. Revie and Uhlig [33] ascribed the observed lag in the creep response to diffusional process of vacancies that were created very near the metal surface associated with metal dissolution [34]. Divacancies diffusing from the surface were assumed to interact with sessile dislocations causing climb under applied stress.

On the other hand, cathodic polarization is characterized by an abrupt increase in creep rate and a very small current density of 0.1 A/m^2 resulted in a marked increase of creep rate compared with anodic polarization. Revie and Uhlig ascribed the effect to the reduction of surface energy. Hydrogen generated by cathodic electrolysis adsorbs on the specimen surface preceding the entry into the bulk. The change in surface energy, dγ, of metals caused by a change of the chemical potential, dμ, of an adsorbed phase is given by the Gibbs adsorption isotherm. If the adsorption takes place at temperature T and pressure p,

$$\begin{aligned} d\gamma &= -\Gamma d\mu \\ &= -\Gamma k_B T \ln p, \end{aligned} \tag{5.9}$$

where Γ is the number of molecules adsorbed per unit area and k_B is the Boltzmann constant [35]. For the Langmuir adsorption, *i.e.* monolayer adsorption, of dissociated atoms of diatomic molecules, γ is expressed as

$$\gamma = \gamma_0 - 2\Gamma_s k_B T \ln\left[1 + (Ap)^{1/2}\right], \tag{5.10}$$

where γ_0 is the surface energy without adsorption, Γ_s is the saturation value of Γ and A is a constant. Petch calculated the reduction of γ of α-iron by the adsorption of hydrogen on the crack surface at room temperature, and the results are shown in Fig. 5.8 [35]. The idea and assumptions for the calculation are described in Sect. 9.2 concerning mechanisms of hydrogen embrttlement. The magnitude of γ_0 is about 2 J/m^2 and the fractional reduction of γ shown in Fig. 5.8 is substantial even for very low hydrogen concentrations. Revie and Uhlig postulated that the reduction in surface energy facilitated slip step formations at the metal surface [36]. Since the ease of the slip step formation operates in grains facing the surface, the idea is consistent with the higher acceleration of creep rate for the larger grain size. The

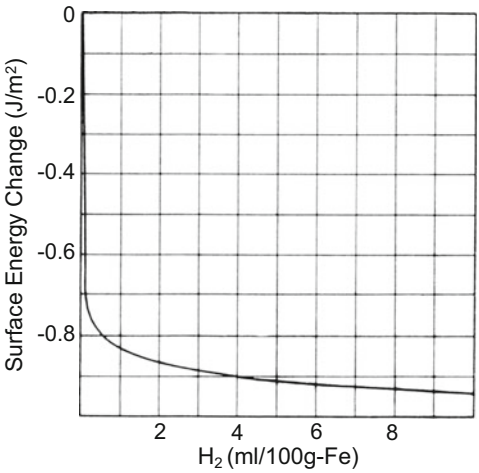

Fig. 5.8 Decrease in the surface energy of iron by adsorption of hydrogen (Petch [35])

idea is also consistent with the fact that the application of cathodic polarization causes a sudden response of creep rate.

If the reduction in surface energy due to adsorbed hydrogen affected creep rate, it also should play a role in stress relaxation. Change of stress states at the surface should alter the balance of internal stress states and induce auxiliary plastic strain. From this notion, the additional plasticity is not a consequence of some direct interactions between hydrogen and dislocations within the bulk phase. In the context, the abrupt drop of the flow stress associated with cathodic polarization on tensile straining, shown in Fig. 5.1, might be ascribed to a decrease in surface energy.

However, Fig. 5.5 that demonstrates the effects of internal hydrogen on stress relaxation implies that surface effects, if any, are not the sole origin of hydrogen effects on creep and stress relaxation. Another candidate mechanism is interactions between hydrogen and strain-induced vacancies. Vacancy formation associated with cathodic electrolysis or dissociation of water molecule at the surface of pure aluminum was observed by Birnbaum et al. [36]. Small angle X-ray scattering and measurements of lattice parameters showed the formation of hydrogen-vacancy complexes clustered into platelets lying on the {111} planes. Candidate origins of vacancies are interactions of moving dislocations as well as possible products on the surface in the case of anodic polarization.

5.4 Direct Observation of Dislocation Activity

The decrease in flow stress shown in Fig. 5.1 and the enhanced stress relaxation shown in Figs. 5.4 and 5.5 lead to the notion of hydrogen-enhanced plasticity. Strong supports of the notion have been obtained by means of in situ environmental

cell transmission electron microscopy. The first observation was for iron foils stretched to a constant displacement initially in vacuum and successively in hydrogen gas introduced into the environmental cell [37]. Increase in the hydrogen gas pressure up to 35 kPa increased the velocity of screw dislocations and the removal of the gas rapidly decreased dislocation velocity to the initial value in vacuum. Similar results were observed for a variety of metals and alloys of bcc, fcc and hcp structures [38]. For high purity aluminum, the introduction of hydrogen increased the length of screw components at the intersection of two slip planes and decreased the length of mostly edge components [39]. It was deduced then that pinning by hydrogen stabilized edge segments of dislocations and decreased the tendency to cross-slipping [39]. For nickel, detailed observations showed that hydrogen increased the dislocation velocity and the generation rate of both isolated and tangled dislocations [40]. Increases in dislocation velocity observed for dislocations lying in tangles and for dislocations emanating from crack tips were ascribed to a volumetric rather than a surface phenomenon. It is to be noticed, however, that the stress balance in the specimen may transmit alteration of surface states to that of internal dislocation structures without the entry of hydrogen.

Enhanced strain localization is another feature of hydrogen effects. In situ observations revealed the crack propagation associated with the emission of dislocations from the crack tips [41]. Generation of dislocations in the vicinity of dislocation cell walls ahead of the crack tip was also observed. Initially formed and arrested cracks in iron foil in vacuum restarted by introducing hydrogen gas into the environmental cell at a stress lower than that in vacuum. Deformation was highly localized near the crack tip and resulted in the formation of small voids. The observations have served as an experimental basis of the hydrogen enhanced localized plasticity (HELP) mechanism of hydrogen embrittlement described in Sects. 5.5 and 10.2.

Hydrogen fugacity expected in environment cell is much lower than the threshold fugacity for stress relaxation observed for a carbon steel [25]. Concentrations of solute hydrogen estimated from Sieverts' law are very low compared with other alloying elements or impurities that alter deformation behaviors of steels. It is to be noticed that most dislocations arrays observed by transmission electron microscopy are initially pinned at the surface of the foil specimen. It is feasible that a substantial decrease in surface energy caused by the adsorption of very small amount of hydrogen, as shown in Fig. 5.8, alters the mechanical balance and induces movements of unpinned dislocations.

5.5 Elastic and Atomistic Calculations

5.5.1 Elastic Shielding of Stress Centers

The elastic interaction energy between a hydrogen atom and an edge dislocation originating in the volumetric effect is described in Sect. 3.1.2. The enhancement of

dislocation mobility by hydrogen, revealed by in situ transmission electron microscopy, is quite general for fcc, bcc and hcp crystal structures and also for both edge and screw types of dislocations. Some qualitative explanations of experimental observations are described in Sect. 5.2(c), and a quantitative estimation has been made about the reduction of barriers against dislocation motion.

The mobility of dislocations is affected by elastic interactions between dislocations and between dislocations and other stress centers such as solute atoms and precipitates. Hydrogen atmospheres are formed in the dilatational fields so as to make the energy of the system minimum. Sofronis and Birnbaum calculated effects of hydrogen on the dislocation mobility taking into account both the first order dilatational interaction energy expressed by Eq. (3.8) for an edge dislocation and a second order interaction energy that arises from the change in the elastic moduli caused by the presence of hydrogen in solid solution [38, 42].

Calculations were conducted for various configurations and types of elastic centers. Figure 5.9 [38, 42] is a schematic illustration of the coordinates of interacting two edge dislocations of the same sign and hydrogen atmosphere. The shear stress due to hydrogen atmosphere in the area dS is denoted as $d\tau_H$. The net shear stress, τ_H, acting at the core of the dislocation #2 due to the hydrogen atmosphere of the local concentration $C(r, \varphi)$ is given regarding to the hydrogen volumetric effect as

$$\tau_H = -\frac{\mu}{2\pi(1-\nu)}\frac{V_H}{N_A}\int_0^{2\pi}\int_{r_2}^{R} C(r,\varphi)\frac{\sin 2\varphi}{r}drd\varphi, \tag{5.11}$$

where μ is the shear modulus, ν is Poisson's ratio, V_H is the partial molar volume of hydrogen, N_A is Avogadro's number, r_2 is the inner cut-off radius of the dislocation 2 and R is the outer cut-off radius of the atmosphere centered at the dislocation #2. It is to be noticed that $C(r, \varphi)$ is the hydrogen distribution in equilibrium with an applied stress field and also with stress fields due to the dislocations #1 and #2. The shear stress τ_D resolved along the slip plane and exerted by the dislocation #1 at the core of the dislocation #2 is

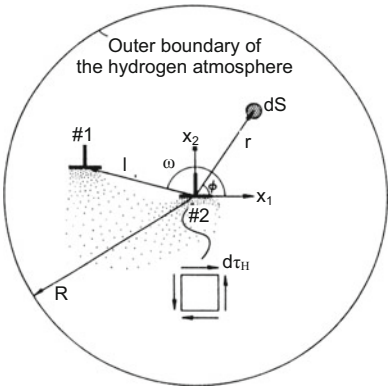

Fig. 5.9 Schematic model for the shear stress acting at the core of dislocation #2 by the hydrogen dilatation lines of an infinitesimal area dS at the position (r, φ) (Birnbaum et al. [38])

$$\tau_D = -\frac{b_1}{2\pi(1-v)}\frac{\cos\omega\cos 2\omega}{l}, \tag{5.12}$$

where b_1 is the Burgers vector of the dislocation 1. The net shear stress exerted on the dislocation #2 is equal to $\tau_D + \tau_H$.

Figure 5.10 [38, 42] plots calculated normalized shear stresses, τ_H/μ, τ_D/μ and $(\tau_D + \tau_H)/\mu$, *vs.* normalized distance, l/b, and nominal hydrogen concentrations of H/M = 0.1 and 0.01 for bcc niobium at 300 K. Figure 5.10 indicates that hydrogen atmosphere reduces the repulsive interaction between parallel edge dislocations of the same sign. Very similar results were also obtained for two dislocations of opposite signs. Calculated elastic energies of edge dislocations with and without hydrogen atmospheres are shown in Fig. 5.11 [39] for aluminum as a function of nominal hydrogen concentration. The energies are expressed as the energy per atomic distance along the dislocations. In both Figs. 5.10 and 5.11, fairly high

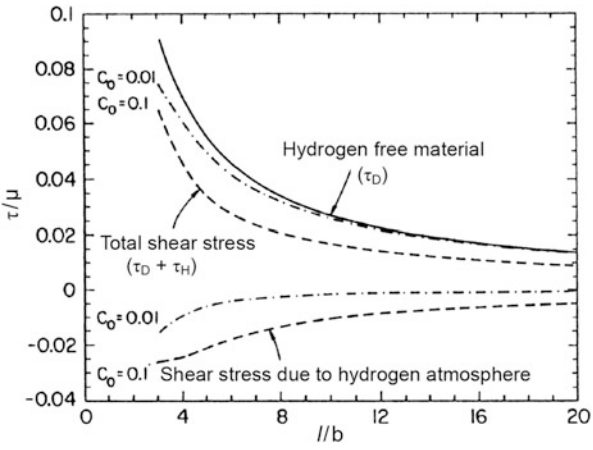

Fig. 5.10 The normalized shear stress due to hydrogen, τ_H/μ, and due to dislocation #1, τ_D/μ, and net shear stress, $(\tau_D + \tau_H)/\mu$, at the core of dislocation #2 at 200 K and nominal hydrogen concentrations of H/M = 0.1, 0.01 in Nb (Sofronis et al. [42])

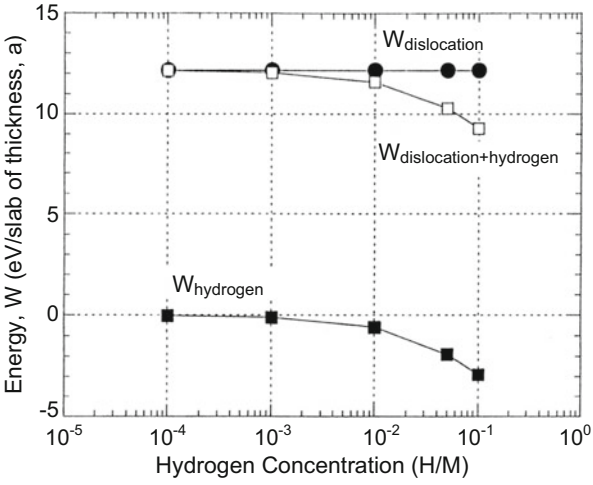

Fig. 5.11 Calculated elastic energies of edge dislocations with and without hydrogen atmospheres as a function of hydrogen concentrations. The energies are given as energy per atomic distance along the dislocation (Ferreira et al. [39])

hydrogen concentrations over 0.01 are necessary to exhibit the shielding effects by hydrogen. Ferreira et al. postulated that the formation of hydrogen atmosphere around edge components of dislocations decreased the energy of the system and disturbed cross-slipping [39]. However, low hydrogen gas pressure in the environmental cell is unlikely to realize such a high hydrogen concentration.

For screw dislocations, direct interactions with hydrogen are very weak because of a cubic symmetry of the deformation field around a hydrogen atom. Sofronis and Birnbaum showed that hydrogen shielding operates also in elastic interactions between dislocations and carbon atom. Screw dislocations interact with carbon atoms. Then, the stress acting on screw dislocations as well as edge dislocations are affected by hydrogen as a result of interactions between hydrogen and carbon atoms [38, 42]. Sofronis and Birnbaum calculated the interaction energy between a dislocation and a carbon atom in the presence of hydrogen atmosphere. A finite element method calculation was conducted taking into account the modulus change of the carbon atom by hydrogen atmosphere as shown in Eq. (5.13) using data for niobium [43],

$$E = E_0(1 + 0.34c), v = v_0 - 0.025c, \mu = \mu_0 \frac{1 + 0.34c}{1 - 0.0177c}. \tag{5.13}$$

The results are complicated, either increase or decrease in the interaction energy depending on the locations and tetragonal axes of the carbon atom. The modulus effect is a weak second order interaction operating in a short range. Hydrogen effects were prominent when the carbon atom locates very close, within one Burgers vector, to the dislocation core. Also, the calculations were for the case of a very high nominal hydrogen concentration of H/M = 0.1.

On the other hand, atomistic modellings for the edge dislocation mobility and pile-ups showed hydrogen effects against shielding of elastic fields [44]. Large-scale molecular dynamics simulations were conducted by applying shear stress to a cell composed of bcc iron and three edge dislocations with/without hydrogen precharging. The formation of the Cottrell atmosphere of hydrogen around moving dislocations was derived, and the pile-up structures were not affected by hydrogen. The results imply that the mobility of edge dislocation is reduced by the drag of hydrogen and that the hydrogen atmosphere provides no measurable shielding of dislocation interactions.

5.5.2 *Mobility of Screw Dislocations – Atomistic Calculations*

First-principles calculations on interactions between hydrogen and screw dislocation core are described in Sect. 3.1.2. The nucleation of kink-pair and its expansion control the movement of screw dislocation. Wen et al. calculated the effects of hydrogen on the nucleation and the sideward movement energies of kink-pairs in bcc iron [45]. Assuming the kink nucleation on 1/2[111] screw dislocation to take

place at a hydrogen atom, binding energies of hydrogen were calculated for various sites of hydrogen in the core. Kinking processes were determined so as to take the minimum energy path during the expansion along the dislocation meeting and overcoming another hydrogen atom. The activation energy of kinking was expressed in terms of the maximum of the increased energy of the dislocation during kinking process.

Softening by hydrogen, *i.e.* reduction in the activation energy, appeared in the sideward movement rather than in the nucleation of a kink pair when the hydrogen state changed from a weaker trapped site to a stronger one. The maximum reduction by hydrogen was about 20 % of about 100 kJ/mol of the overall increase in the dislocation energy in the kinking process. However, softening was not always the case in the kinking process. Hardening was expected when the transition was from a stronger to a weaker trapped site. When hydrogen sites before and after kinking were of the same binding energy, hydrogen effects did not appear in kinking. The sideward motion of a kink pair is impeded when the kink pair meets hydrogen thus inducing hardening.

Itakura et al. conducted a density functional theory calculation of the kink pair nucleation enthalpy H_k in bcc iron using a line tension model of a curved dislocation with/without hydrogen [46]. Two types of the core configuration, stable or unstable, were assumed for screw dislocation and hydrogen atoms were placed at various *T*-sites near the core. Movement of a screw dislocation required alternation of the two core configurations with the saddle point of the migration path close to the unstable configuration. The enthalpy of a curved dislocation incorporated the position energy of the core, the Peierls barrier, the contributions of external stress and the interaction energy between the dislocation line and hydrogen atoms.

Hydrogen enhances the kink nucleation rate by reducing H_k. The calculated H_k was a function of applied stress, decreasing from 700 kJ/mol to zero as shear stress up to 1000 MPa was applied [46]. The effect of hydrogen in reducing H_k was about 11 kJ/mol for all levels of applied stress. The velocity of screw dislocation was determined by the kink nucleation rate. In order that softening takes place, a sufficient trapping of hydrogen must occur at moving kinks. Itakura et al. showed a region in the temperature-stress diagram where the screw dislocation velocity was increased by hydrogen in bcc iron [46]. Figure 5.12 [46] shows the region for 0.1 at.

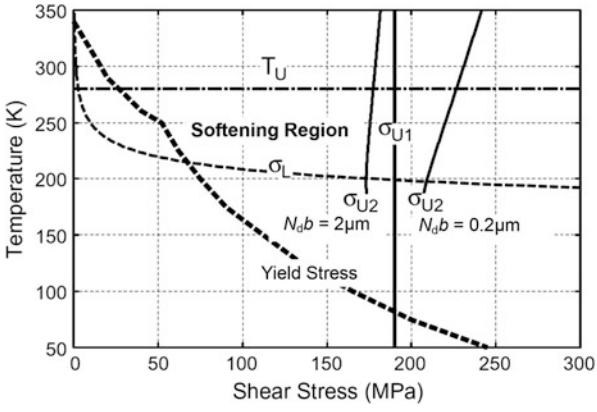

Fig. 5.12 A region in the temperature-stress diagram where an increase in the screw dislocation velocity by solute hydrogen is possible. Calculation for 0.1 at. ppm of hydrogen and two dislocation lengths of 2.0 and 0.2 μm (Itakura et al. [46])

ppm of hydrogen in solid solution. The region is bounded by the upper critical temperature T_U, the lower critical stress σ_L, the yield stress and two kinds of upper critical stress σ_{U1} and σ_{U2}. Two upper critical stresses limit the movements of the dislocation and the kink so as to keep the hydrogen concentration together with. The activation of screw dislocations against trapping of kink by hydrogen required large applied shear stress. Values of σ_{U2} were calculated for two typical dislocation lengths denoted as N_d in unit of the Burgers vector b. Also, the upper critical temperature was determined to keep the hydrogen concentration at the promotion sites. The temperature ranges are almost consistent with experimental flow stress behaviors shown in Sect. 5.2, while exact hydrogen concentrations are not definite.

In Sect. 3.2, the generation of vacancies associated with dragging of jogs on screw dislocations and its enhancement by hydrogen is described. The velocity of jog under applied stress is a function of the sum of the formation and the migration energies of vacancies. Matsumoto et al. noticed that hydrogen effects on the two energies almost cancel and the velocity of jogs is not affected by the presence of hydrogen [47]. Hydrogen effects on jog dragging are to increase the density of created vacancies by suppressing the diffusion of vacancies.

References

1. H.A. Wriedt, R.A. Oriani, Scr. Metall. **8**, 203–208 (1974)
2. N.E. Paton, O. Buck, J.C. Williams, Scr. Metall. **9**, 687–691 (1975)
3. E. Lunarska, A. Zielinski, M. Smialowski, Acta Metall. **25**, 305–308 (1977)
4. S. Matsuyama, in *Report of Studies on the Mechanism of Delayed Fracture* (Iron and Steel Institute of Japan, Tokyo, 1975), pp. 113–124
5. A. Goumelon, Mem. Sci. Rev. Mét. **72**, 475–489 (1975)
6. A. Kimura, H. Matsui, H. Kimura, in *Hydrogen in Metals*, Suppl. Trans. JIM **21**, 541–544 (1980)
7. M. Cornet, S. Talbot-Besnard, in *Hydrogen in Metals*, Suppl. Trans. JIM **21**, 545–548 (1980)
8. Y. Tobe, W.R. Tyson, Scr. Metall. **11**, 849–852 (1977)
9. I.M. Bernstein, Scr. Metall. **11**, 343–350 (1977)
10. S. Asano, Y. Nishino, M. Otsuka, J. Jpn. Inst. Metals **43**, 241–248 (1979)
11. S. Moriya, H. Matsui, H. Kimura, Mater. Sci. Eng. **40**, 217–225 (1979)
12. H. Matsui, H. Kimura, S. Moriya, Mater. Sci. Eng. **40**, 207–216 (1979)
13. H. Kimura, H. Matsui, A. Kimura, in *Hydrogen in Metals*, Suppl. Trans. JIM **21**, 533–540 (1980)
14. H. Matsui, H. Kimura, A. Kimura, Mater. Sci. Eng. **40**, 227–234 (1979)
15. H. Wada, S. Sakamoto, in *Hydrogen in Metals*, Suppl. Trans. JIM **21**, 553–556 (1980)
16. R.A. Oriani, P.H. Josephic, Metall. Trans. A **11A**, 1809–1820 (1980)
17. E. Lunarska, V. Novak, N. Zarubova, S. Kadeckova, Scr. Metall. **17**, 705–710 (1983)
18. C.G. Park, K.S. Shin, J. Nakagawa, M. Meshii, Scr. Metall. **14**, 279–284 (1980)
19. C.D. Beachem, Metall. Trans. **3**, 437–451 (1972)
20. E. Furubayashi, J. Phys. Soc. Jpn. **27**, 130–140 (1969)
21. A.S. Keh, Philos. Mag. **12**, 9–30 (1965)
22. W.G. Johnston, J.J. Gilman, J. Appl. Phys. **30**, 129–144 (1959)
23. I. Gupta, J.C.M. Li, Metall. Trans. **1**, 2323–2330 (1970)
24. E. Lunarska, Scr. Metall. **11**, 283–287 (1977)

25. R.A. Oriani, P.H. Josephic, Acta Metall. **27**, 997–1005 (1979)
26. M. Nagumo, T. Tamaoki, T. Sugawara, in *Hydrogen Effects on Materials Behavior and Corrosion Deformation Interactions*, ed. by N.R. Moody, A.W. Thompson, R.E. Ricker, C.W. Was, K.H. Jones (TMS, Warrendale, 2003), pp. 999–1008
27. T. Fujita, T. Sakai, in *Report of Studies on the Mechanism of Delayed Fracture* (Iron and Steel Institute of Japan, Tokyo, 1975), pp. 189–199
28. M. Nagumo, Y. Monden, in *Report of Studies on the Mechanism of Delayed Fracture* (Iron and Steel Institute of Japan, Tokyo, 1975), pp. 149–164
29. A.H. Cottrell, *Dislocations and Plastic Flow in Crystals*, Chap. 16 (Oxford University Press, London, 1956)
30. A.H. Cottrell, Philos. Mag. Lett. **82**, 65–70 (2002)
31. R.A. Oriani, P.H. Josephic, Acta Metall. **29**, 669–674 (1981)
32. Z.R. Xu, R.B. McLellan, Acta Mater. **46**, 4543–4547 (1998)
33. R.W. Revie, H.H. Uhlig, Acta Metall. **22**, 619–627 (1974)
34. D.A. Jones, Metall. Trans. A **16A**, 1133–1141 (1985)
35. N.J. Petch, Philos. Mag. **1**, 331–337 (1956)
36. H.K. Birnbaum, C. Buckley, F. Zeides, E. Sirois, P. Rozenak, S. Spooner, J.S. Lin, J. Alloys Compds. **253-254**, 260–264 (1997)
37. T. Tabata, H.K. Birnbaum, Scr. Metall. **17**, 947–950 (1983)
38. H.K. Birnbaum, P. Sofronis, Mater. Sci. Eng. **A176**, 191–202 (1994)
39. P.J. Ferreira, I.M. Robertson, H.K. Birnbaum, Acta Mater. **47**, 2991–2998 (1999)
40. I.M. Robertson, H.K. Birnbaum, Acta Metall. **34**, 353–366 (1986)
41. T. Tabata, H.K. Birnbaum, Scr. Metall. **18**, 231–236 (1984)
42. P. Sofronis, H.K. Birnbaum, J. Mech. Phys. Solids **43**, 49–90 (1995)
43. F.M. Mozzolai, H.K. Birnbaum, J. Phys. F: Met. Phys. **15**, 507–523 (1985)
44. J. Song, W.A. Curtin, Acta Mater. **68**, 61–69 (2014)
45. M. Wen, S. Fukuyama, K. Yokogawa, Acta Mater. **51**, 1767–1773 (2003)
46. M. Itakura, H. Kaburaki, M. Yamaguchi, T. Okita, Acta Mater. **61**, 6857–6867 (2013)
47. R. Matsumoto, N. Nishiguchi, S. Taketomi, N. Miyazaki, J. Soc. Mater. Sci. Jpn. **63**, 182–187 (2014)